Energy & Environmental Science

ROYAL SOCIETY OF CHEMISTRY

PAPER

View Article Online
View Journal | View Issue

Check for updates

Cite this: *Energy Environ. Sci.*, 2026, **19**, 860

Machine learning-accelerated discovery of multi-cation entropy-stabilized NASICON solid electrolytes with 10 000 hours of stable Na plating/stripping for all-solid-state sodium batteries

Daxian Zuo,†[ab] Jiaming Tian,†[a] Yu Sun,†[a] Xin Yu,[a] Bo Peng,[a] Tao Yu,[ab] Chengrong Xu,[ab] Xiangqun Xu,[ab] Yigang Wang,[a] Yiwen Liu,[a] Tianze Shi,[a] Yinhui Feng,[a] Jie Yang,[a] Haoshen Zhou [a] and Shaohua Guo *[ab]

The application of medium-/high-entropy materials has revolutionized the design of solid-state electrolytes (SSEs) by stabilizing single-phase solutions from otherwise incompatible elements. However, navigating the vast compositional space of entropy-stabilized materials remains a significant challenge. To overcome this, we introduce a machine learning (ML)-accelerated approach to identify multi-cation NASICON oxide SSEs. By training a Gaussian Naive Bayes model on four key descriptors (ionic radius, electronegativity, valence state, and configurational entropy), we found four promising compositions incorporating Zr, Ti, Hf, Lu, Ga, and Sc. These compositions exhibit notable entropy-driven stabilization, demonstrated by the complete suppression of Na_3PO_4/ZrO_2 impurity formation. Among them, the medium-entropy phase $Na_{3.5}Zr_{1.0}Ti_{0.5}Lu_{0.5}Si_2PO_{12}$ achieved remarkable performance, delivering an ionic conductivity of 1.3 mS cm^{-1} at room temperature, a critical current density of 1.9 mA cm^{-2}, and over 10 000 hours of stable Na plating/stripping. When integrated into all-solid-state sodium batteries with a high-voltage $Na_3V_2(PO_4)_2F_3$ cathode and a sodium anode, it further demonstrated exceptional battery performance indicators, including high-rate capability (110 mAh g^{-1} at 5C) and long-term cycling stability (80% capacity retention after 700 cycles at 2C). This work establishes entropy engineering, coupled with ML guidance, as a powerful paradigm for the rational design of next-generation SSEs.

Received 3rd November 2025,
Accepted 14th January 2026

DOI: 10.1039/d5ee06594a

rsc.li/ees

Open Access Article. Published on 16 janvier 2026. Downloaded on 2026-02-20 16:23:26.
This article is licensed under a Creative Commons Attribution-NonCommercial 3.0 Unported Licence.

Broader context

The transition to renewable energy necessitates the development of safe, high-energy-density, and sustainable energy storage systems. All-solid-state sodium batteries (ASSSBs) represent a promising alternative to conventional lithium-based technologies, owing to the abundance of sodium and enhanced safety. However, the widespread adoption of ASSSBs is hindered by the limitations of existing solid-state electrolytes, particularly in terms of ionic conductivity, phase stability, and interfacial compatibility. NASICON-type electrolytes, while advantageous, suffer from inherent issues such as impurity formation and restricted Na^+ transport pathways. This work introduces a machine learning-accelerated strategy to design entropy-stabilized multi-cation NASICON materials, effectively addressing these challenges. By combining computational intelligence with advanced synthesis and characterization, we demonstrate a novel electrolyte with exceptional ionic conductivity and unprecedented cycling stability. Our approach not only advances the fundamental understanding of entropy regulation in ion-conducting materials but also provides a scalable pathway toward next-generation, high-performance solid-state batteries, with implications extending to Li^+, K^+, and multivalent-ion systems.

Introduction

The rapid development of renewable energy systems and the growing demand for grid-scale energy storage have intensified the search for next-generation battery technologies that combine high energy density, intrinsic safety, and cost-effectiveness.[1–5] All-solid-state sodium batteries (ASSSBs) have emerged as

[a] College of Engineering and Applied Sciences, Jiangsu Key Laboratory of Artificial Functional Materials, National Laboratory of Solid-State Microstructures, Collaborative Innovation Centre of Advanced Microstructures, Nanjing University, Nanjing 210093, China. E-mail: shguo@nju.edu.cn
[b] Lab of Power and Energy Storage Batteries, Shenzhen Research Institute of Nanjing University, Shenzhen 518000, China
† These authors contributed equally to this work.

This journal is © The Royal Society of Chemistry 2026

Open Access Article. Published on 16 janvier 2026. Downloaded on 2026-02-20 16:23:26.
This article is licensed under a Creative Commons Attribution-NonCommercial 3.0 Unported Licence.

particularly promising candidates to meet these requirements, offering several advantages over conventional lithium-ion systems, including the abundance of sodium resources, reduced flammability risks, and wider operational temperature ranges.[6–8] At the heart of ASSSB performance lies the solid-state electrolyte (SSE),[9–11] which must simultaneously satisfy stringent requirements for ionic conductivity, electrochemical stability, and mechanical robustness. Among various SSE candidates, NASICON-type oxides (Na super ionic conductors) have attracted considerable attention due to their unique combination of high Na^+ conductivity (10^{-4}–10^{-3} S cm^{-1} at room temperature), excellent chemical stability against sodium metal, and relatively low synthesis costs compared to halide- and sulfide-based alternatives.[12–14]

Despite these advantages, conventional NASICON electrolytes like $Na_3Zr_2Si_2PO_{12}$ (NZSP) face several fundamental challenges that limit their practical application.[15–17] The high-temperature solid-state synthesis (typically $\geq$1100 °C) often leads to the formation of ZrO_2 impurities and sodium volatilization, both of which significantly degrade ionic transport properties.[18–20] Furthermore, the limited configurational flexibility in single-cation frameworks restricts opportunities for optimizing Na^+ migration pathways.[21,22] Recent studies have demonstrated that partial substitution of Zr^{4+} with aliovalent cations (*e.g.*, Zn^{2+}, Pr^{3+}, Eu^{3+}) can enhance conductivity to some extent, but these modifications often compromise phase stability or introduce new impurity phases.[23,24] These challenges highlight the need for innovative design strategies that can simultaneously address multiple material limitations.

The emerging field of medium-/high-entropy materials (characterized by configurational entropy values of 1.0–1.5R for medium entropy and above 1.5R for high entropy, where R is the gas constant) has revolutionized materials design by demonstrating that configurational entropy stabilization can suppress phase separation and enable novel functional properties.[25–27] This principle has been successfully applied to various material classes, including alloys,[28–30] ceramics,[31,32] and recently, lithium-ion conductors.[33,34] For sodium-ion conductors, entropy stabilization strategies have shown significant progress in NASICON-type cathodes (*e.g.*, multi-cation-substituted $Na_3V_2(PO_4)_3$),[35–37] where medium-/high-entropy compositions enhance structural stability and electrochemical performance. However, critical gaps remain in understanding entropy effects in NASICON oxide SSEs. The concept of medium-/high-entropy NASICON oxide SSEs presents an intriguing opportunity to balance entropy stabilization effects with practical synthesis constraints, but the enormous compositional space makes traditional experimental approaches prohibitively time-consuming. This necessitates a paradigm shift toward data-driven material discovery.

Machine learning (ML) has emerged as a powerful tool to accelerate materials discovery by identifying composition-property relationships in high-dimensional spaces. Recent successes include the prediction of novel battery materials,[38,39] catalysts,[40–42] and photovoltaic compounds.[43,44] However, the use of ML to design synthesizable medium-/high-entropy ionic conductors–particularly in NASICON-type sodium SSEs–remains largely unexplored, with few studies addressing the challenge of predicting phase-stable multi-cation compositions. The lack of comprehensive datasets and appropriate descriptor selection for medium-/high-entropy materials further complicates this challenge.

This work presents a ML-guided strategy for designing synthesizable medium-/high-entropy NASICON-type oxide SSEs. In contrast to traditional synthesis methods, our approach offers rational design framework, a predictable design space, as well as high efficiency and cost-effectiveness (Fig. 1). By employing gaussian naive bayes algorithms, we identified four multi-cation compositions that utilize entropy stabilization to improve both phase purity and ionic conductivity. Key innovations include the development of effective descriptors for predicting phase stability, quantitative correlations between configurational entropy and impurity suppression, and mechanistic insights into how multi-cation substitution enhances Na^+ transport. Among the candidates, the synthesized medium-entropy $Na_{3.5}Zr_{1.0}Ti_{0.5}Lu_{0.5}Si_2PO_{12}$ exhibited a high room-temperature ionic conductivity of 1.3 mS cm^{-1}–five times higher than that of conventional NZSP–and demonstrated long-term Na plating/stripping stability in symmetric cells (10 000 hours at 0.1 mA cm^{-2}). Moreover, assembled ASSSBs demonstrated excellent electrochemical performance when paired with a high-voltage $Na_3V_2(PO_4)_2F_3$ (NVPF) cathode and a sodium anode, delivering 110 mAh g^{-1} at 5C and retaining 80% of capacity after 700 cycles at 2C. This study demonstrates the successful application of ML in designing entropy-stabilized ionic conductors, establishes fundamental entropy-property relationships, and provides a generalizable framework for accelerating the discovery of advanced energy materials.

Results and discussion

ML-driven composition design of medium-/high-entropy NASICON oxide SSEs

The successful design of medium- and high-entropy NASICON oxide SSEs was enabled by a carefully developed ML framework, as illustrated in Fig. 2a. The dataset consisted of 58 distinct NASICON-type compositions (Table S1), including both previously reported materials and newly proposed candidates. Each composition was labeled as either ''synthesizable'' or ''non-synthesizable'' based on experimental phase analysis. To capture the key factors influencing phase stability, we selected four critical descriptors (Table S2): (1) ionic radius (ranging from 70.13 to 86.98 pm), (2) electronegativity (1.204 to 1.786), (3) valence state (3.20 to 4.00), and (4) configurational entropy (ΔS_{mix} = 0.199R to 1.609R). These features were chosen due to their well-established impact on cation miscibility and structural stability in oxide systems.[45–48] Using these four descriptors, ML-based predictions were generated and fed back into the database, forming a closed-loop feedback mechanism to iteratively improve the model. We assessed the performance of five supervised ML algorithms–*k*-nearest neighbors (KNN),

Open Access Article. Published on 16 janvier 2026. Downloaded on 2026-02-20 16:23:26.
This article is licensed under a Creative Commons Attribution-NonCommercial 3.0 Unported Licence.

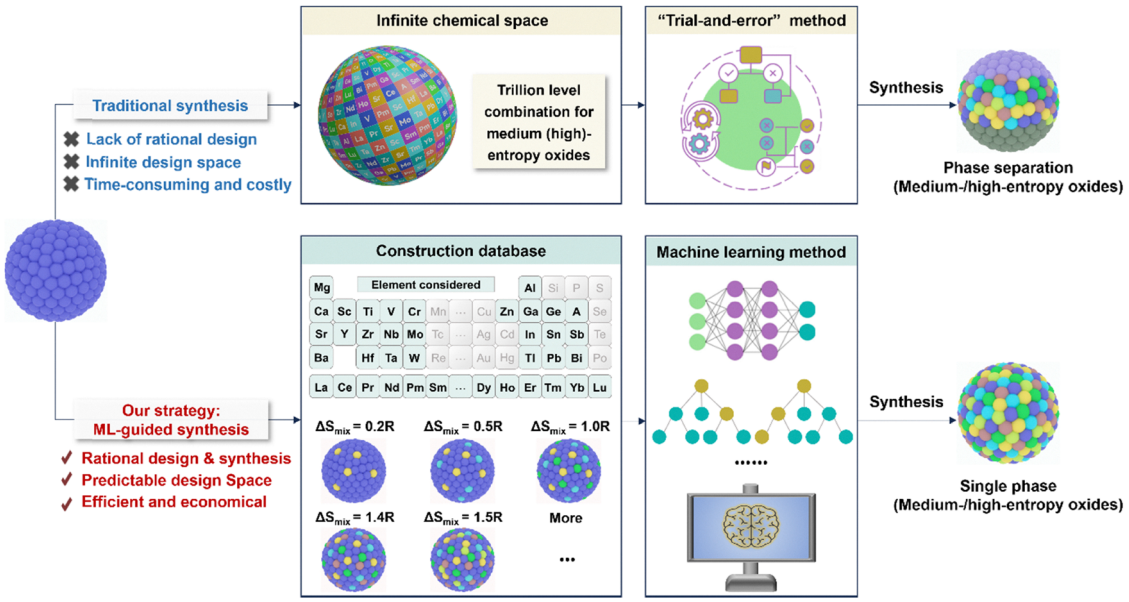

Fig. 1 Schematic of the discovery process for medium-/high-entropy oxides. Comparative advantages of ML-guided synthesis *versus* conventional methods for developing medium-/high-entropy NASICON-type oxide SSEs.

decision tree (DT), support vector machine (SVM), Gaussian naive Bayes (GNB), and multilayer perceptron (MLP) – *via* 10-fold cross-validation (Fig. 2b). Among them, the GNB model achieved the highest prediction accuracy of 92.3%, significantly outperforming the other four algorithms (KNN: 61.5%; DT: 69.2%; SVM: 84.6%; MLP: 69.2%).

To further evaluate the predictive capability and robustness of the models, comprehensive performance analyses were conducted. As shown in Fig. S1, the confusion matrices provide a detailed breakdown of the classification performance for each model. Compared to the other models, the GNB model demonstrates a superior balance with the highest number of true

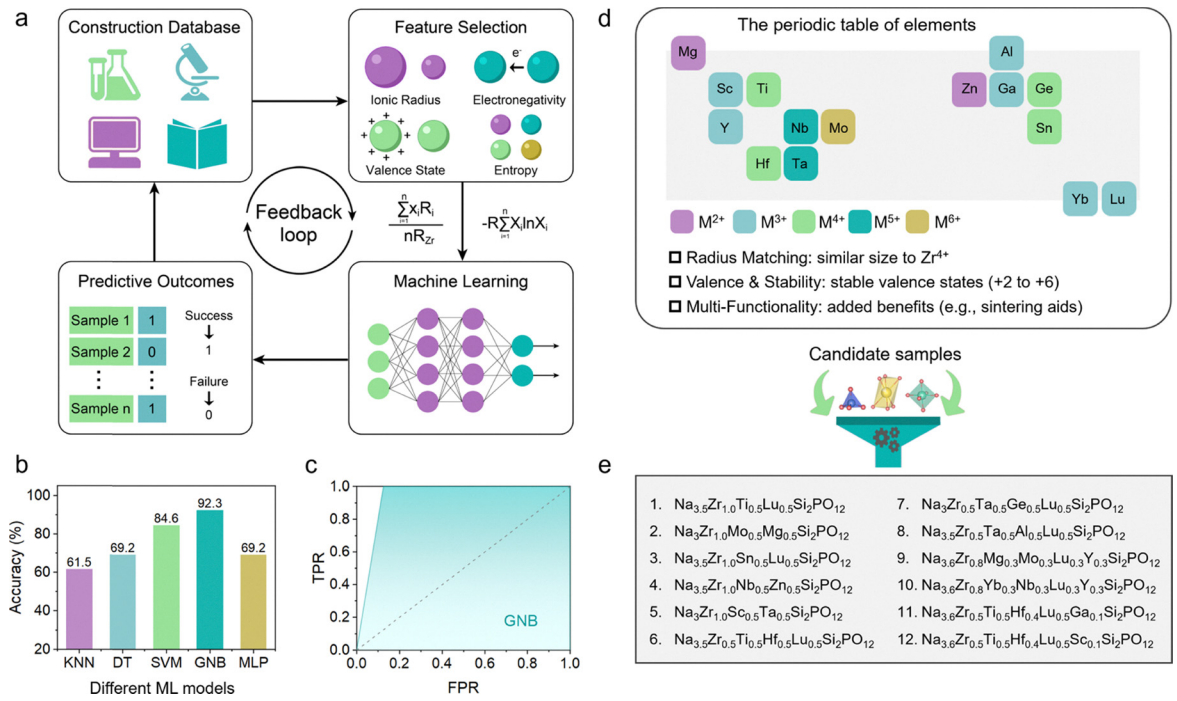

Fig. 2 Composition design of medium-/high-entropy NASICON oxide SSEs. (a) Schematic workflow of ML-assisted synthesis prediction for medium-/high-entropy NASICON oxide SSEs. (b) Test accuracy of various machine learning models: KNN, DT, SVM, GNB, and MLP. (c) The ROC curves of GNB model. (d) Types and selection criteria for medium-/high-entropy dopant elements. (e) Twelve designed medium- to high-entropy compositions for prediction.

 This journal is © The Royal Society of Chemistry 2026

Open Access Article. Published on 16 janvier 2026. Downloaded on 2026-02-20 16:23:26.
This article is licensed under a Creative Commons Attribution-NonCommercial 3.0 Unported Licence.

positives and true negatives, corroborating its top accuracy. The ROC curves (Fig. 2c and Fig. S2) offer additional insight into the models' diagnostic ability across all classification thresholds. The GNB classifier again excels, with its curve occupying the uppermost left position and achieving the largest area under the curve (AUC), indicative of excellent distinguishability between synthesizable and non-synthesizable compositions. The SVM model also shows a strong performance, though slightly inferior to GNB, while the curves for KNN, DT, and MLP are closer to the diagonal, reflecting a lower predictive power. Furthermore, the feature importance was evaluated by measuring the increase in model error when each individual descriptor was removed from the training process. A larger increase in error indicates a stronger contribution of that feature to the predictive performance of the model (Fig. S3). The results identified configurational entropy and ionic radius as the two most influential features, indicating their dominant role in determining the synthesizability of medium- and high-entropy NASICON oxides. Other descriptors, such as valence state and electronegativity, also contributed meaningfully but to a lesser extent.

The selection of dopant elements for medium- and high-entropy NASICON materials was guided by three key criteria (Fig. 2d): (1) ionic radius matching with Zr^{4+} to maintain structural stability, (2) incorporation of elements with stable valence states ranging from +2 to +6 to enable precise control of sodium concentration, and (3) inclusion of multi-functional cations (*e.g.*, Nb, Ta) to enhance sintering and electrochemical properties. Using GNB algorithm, we predicted twelve medium- and high-entropy oxide compositions (Fig. 2e). As summarized in Table S3, the predictions showed good agreement with experimental results for eleven of the twelve compositions. The only exception was $Na_{3.5}Zr_{1.0}Sn_{0.5}Lu_{0.5}Si_2PO_{12}$, which was not successfully predicted. As shown in Fig. S4, the ML model identified four synthesizable SSEs: $Na_{3.5}Zr_{1.0}Ti_{0.5}Lu_{0.5}Si_2PO_{12}$ (ME1-NZSP), $Na_{3.5}Zr_{0.5}Ti_{0.5}Hf_{0.5}Lu_{0.5}Si_2PO_{12}$ (ME2-NZSP), $Na_{3.6}Zr_{0.5}Ti_{0.5}Hf_{0.4}Lu_{0.5}Ga_{0.1}Si_2PO_{12}$ (HE1-NZSP), and $Na_{3.6}Zr_{0.5}Ti_{0.5}Hf_{0.4}Lu_{0.5}Sc_{0.1}Si_2PO_{12}$ (HE2-NZSP).

Solid-state synthesis and structural characterization

The four medium- and high-entropy NASICON oxide SSEs were synthesized *via* a two-stage solid-state reaction using high-purity precursors. The process involved ball-milling, calcination at 900 °C, and sintering at 1100 °C under controlled conditions to ensure phase purity and dense pellet formation. (see Methods for details, SI). Structural characterization by X-ray diffraction (XRD) with Rietveld refinement revealed that all compositions crystallized in a well-defined monoclinic structure with space group *C*2/*c* (Fig. 3a). The refinement patterns showed excellent agreement between observed and calculated intensities ($R_{wp} < 6\%$, $R_p < 4\%$ for all samples). Notably, the6absence of any detectable secondary phases (particularly ZrO_2, which commonly forms in conventional NASICON synthesis[18–20]) validated

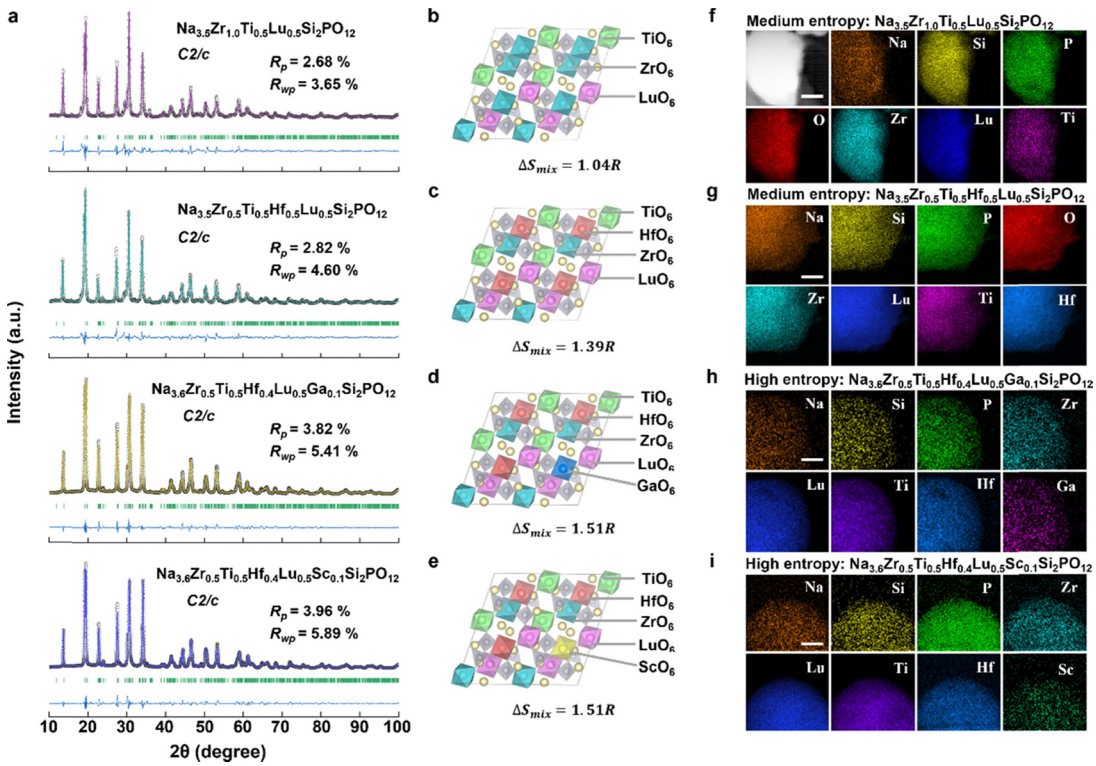

Fig. 3 Solid-state synthesis of medium- and high-entropy NASICON oxide SSEs. (a) XRD Rietveld refinement patterns of four medium-/high-entropy NASICON oxide SSEs. All refined samples have a monoclinic pure phase structure with space group *C*2/*c*. Structural models based on cation substitutions for representing (b) ME1-NZSP, (c) ME2-NZSP, (d) HE1-NZSP, and (e) HE2-NZSP. Elemental mappings of (f) ME1-NZSP, (g) ME2-NZSP, and (h) HE1-NZSP, and (i) HE2-NZSP, showing that the elements are homogeneously distributed. Scale bars are 50 nm.

Open Access Article. Published on 16 janvier 2026. Downloaded on 2026-02-20 16:23:26.
This article is licensed under a Creative Commons Attribution-NonCommercial 3.0 Unported Licence.

the effectiveness of the entropy stabilization approach. The Rietveld-refined structural parameters (Tables S4–S7) reveal systematic variations in lattice dimensions and cation distributions across the four NASICON compositions. ME1-NZSP exhibits the largest unit cell volume (a = 15.61382 Å, b = 9.04419 Å, c = 9.19836 Å), attributed to the combined effects of Zr^{4+} and larger Lu^{3+} (0.86 Å) occupancy at the 8f site. In contrast, HE1-NZSP (with Ga^{3+} substitution) shows significant b-axis contraction (9.01500 Å) due to the smaller ionic radius of Ga^{3+} (0.62 Å), while maintaining phase purity through entropy stabilization (ΔS_{mix} = 1.51R). All compositions display statistically disordered cation mixing at 8f sites (Fig. 3b–e), with radius mismatch (Δr) tolerances up to 0.21 Å in HE1-NZSP (Ga^{3+} *vs.* Hf^{4+}), demonstrating the critical role of configurational entropy in stabilizing these multi-cation frameworks. The total Na^+ content per unit cell remains near stoichiometric values (3.48–3.62), with ME2-NZSP (3.48) and HE2-NZSP (3.62) bracketing the designed compositions. Elemental mapping *via* energy-dispersive X-ray spectroscopy (EDS) confirmed uniform elemental distribution (Fig. 3f–i), with no evidence of cation segregation or secondary phase formation.

Entropy-driven stabilization of NASICON oxide SSEs

The phase purity of NASICON-type SSEs is critical for achieving high ionic conductivity, as secondary phases (*e.g.*, ZrO_2) can block Na^+ transport pathways and impair electrochemical performance.[18–20] Conventional single-cation NZSP often suffers from ZrO_2 impurity formation during high-temperature synthesis (particularly above 1100 °C) due to the thermodynamic instability of the Zr^{4+}-dominated framework.[21,22] To overcome this issue, we employed an entropy stabilization strategy by introducing multiple cations (Ti^{4+}, Hf^{4+}, Lu^{3+}, Ga^{3+}, Sc^{3+}) into the Zr^{4+} sites, thereby increasing the configurational entropy and suppressing phase segregation.

The role of configurational entropy in stabilizing the NASICON phase was systematically investigated by tracking phase evolution as a function of ΔS_{mix}. As shown in Fig. 4a, the pristine NZSP sample exhibits two secondary phases–Na_3PO_4 and ZrO_2–alongside the main NASICON phase. With the incorporation of dopants, the Na_3PO_4 phase diminishes, and the XRD pattern of low-entropy composition $Na_{3.5}Zr_{1.5}Lu_{0.5}Si_2PO_{12}$ (LE-NZSP, ΔS_{mix} = 0.56R) shows only the presence of ZrO_2 as a secondary phase. Notably, when the number of dopants is increased such that ΔS_{mix} exceeds 1.00R, the diffraction peaks associated with ZrO_2 disappear entirely, indicating the formation of a single-phase NASICON. This observation is consistent with the Rietveld refinement results presented in Fig. 3, where all synthesized medium-/high-entropy NASICON compositions crystallize in a pure monoclinic $C2/c$ phase with no detectable secondary phases.

To further verify this trend, we conducted phase evolution studies at different synthesis temperatures for samples with varying entropy values. As shown in Fig. 4b, the pristine NZSP sample exhibits typical NASICON and ZrO_2 phases between 1100 °C and 1200 °C. In the low-entropy LE-NZSP sample, both phases are still observed over the same temperature range, but the intensity of ZrO_2 peaks is notably reduced (Fig. 4c). With further increase in ΔS_{mix} to above 1.00R, corresponding to medium-/high-entropy NZSP compositions, the ZrO_2 phase is entirely suppressed, and only a pure NASICON phase is observed across 1100–1200 °C (Fig. 4d and e). This trend aligns with the classical high-entropy stabilization principle,[49] where higher configurational entropy lowers the Gibbs free energy of a

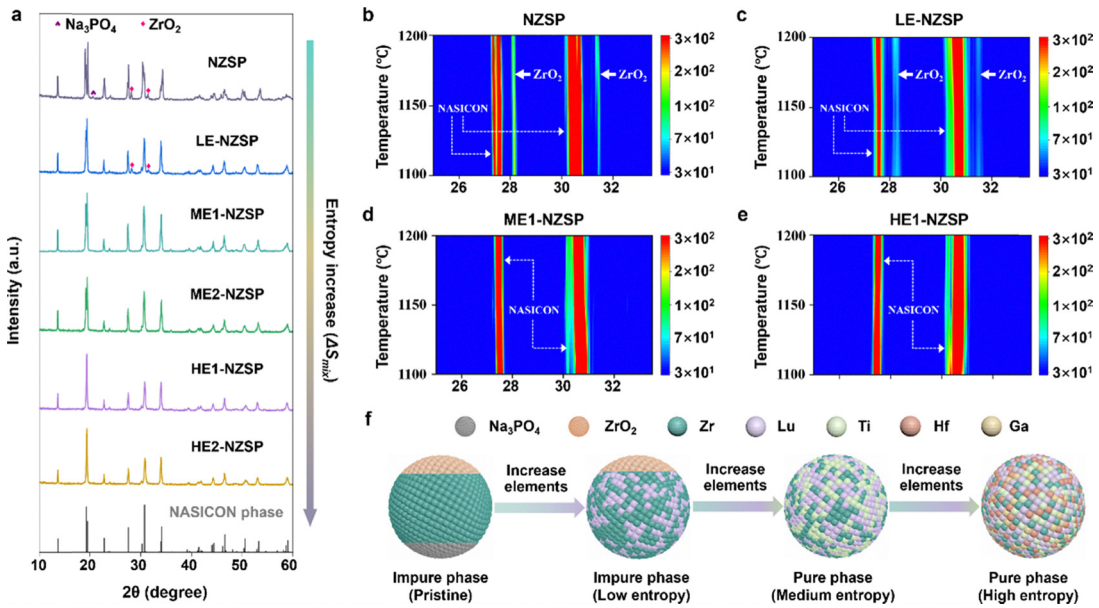

Fig. 4 Entropy-stability effect of NASICON oxide SSEs. (a) XRD patterns of NASICON phase with an increase in configurational entropy. (b)–(e) Phase evolution at different temperatures for (b) pristine NZSP, (c) low-entropy LE-NZSP, (d) medium-entropy ME1-NZSP, and (e) high-entropy HE1-NZSP. Solid white arrows represent the ZrO_2 phase, while dashed white arrows represent the NASICON phase. (f) Schematic of phase evolution showing the increase in configurational entropy with the addition of elements.

 This journal is © The Royal Society of Chemistry 2026

Open Access Article. Published on 16 janvier 2026. Downloaded on 2026-02-20 16:23:26.
This article is licensed under a Creative Commons Attribution-NonCommercial 3.0 Unported Licence.

single-phase solid solution, making it thermodynamically more favorable than phase-separated systems (Fig. 4f). Therefore, increasing configurational entropy effectively suppresses the formation of secondary phases and promotes the stabilization of the NASICON structure.

Ionic transport properties of NASICON oxide SSEs

The ionic transport properties of entropy-stabilized NASICON oxide SSEs were systematically investigated to elucidate the effects of entropy engineering on Na^+ conduction. As shown in Fig. 5a and b, the medium-entropy compositions ME1-NZSP and ME2-NZSP exhibit the highest ionic conductivities, reaching 1.30 mS cm^{-1} and 0.94 mS cm^{-1} at room temperature, respectively. These values significantly outperform those of the high-entropy compositions HE1-NZSP (0.48 mS cm^{-1}) and HE2-NZSP (0.42 mS cm^{-1}), as well as the low-entropy LE-NZSP (0.67 mS cm^{-1}) and the pristine NZSP (0.26 mS cm^{-1}). This demonstrates that entropy engineering can enhance Na^+ transport, with medium-entropy configurations being particularly effective. Additionally, we analyzed the bulk and grain-boundary ionic conductivities of the ME1-NZSP and NZSP samples. As shown in Table S8, both samples exhibit comparable bulk ionic conductivities ($\sim$2.95–2.98 mS cm^{-1}). The most notable improvement is observed in the grain-boundary conductivity. The grain-boundary ionic conductivity for ME1-NZSP (2.16 mS cm^{-1}) is $\sim$7.4 times higher than that of the undoped NZSP (0.29 mS cm^{-1}). This dramatic increase is the primary reason for the superior total ionic conductivity of ME1-NZSP. Therefore, although the bulk conductivities are similar, the vastly improved grain-boundary conductivity directly results in ME1-NZSP achieving a total ionic conductivity (1.30 mS cm^{-1}) that is approximately 5 times higher than that of baseline NZSP (0.26 mS cm^{-1}).

To isolate the effect of multi-cation substitution, we further compared ME1-NZSP with singly doped Ti^{4+}- and Lu^{3+}-containing samples (Fig. 5c), which all showed lower conductivities than ME1-NZSP, confirming the synergistic benefits of multi-element doping. Additionally, a comparison with literature-reported entropy-stabilized NASICON compositions (Fig. 5d) shows that ME1-NZSP achieves the highest ionic conductivity among all reported systems employing an entropy engineering strategy. A primary factor underlying the enhanced conductivity is the reduced activation energy for Na^+ migration. As shown by the Arrhenius plots (Fig. S5), ME1-NZSP exhibits an activation energy of 0.29 eV–significantly lower than that of pristine NZSP (0.35 eV)–indicating that configurational disorder introduced by multi-cation substitution facilitates Na^+ hopping by lowering the migration energy barriers. To further understand the structural origins of this effect, density functional theory (DFT) calculations were performed to optimize the crystal structures of four representative compositions: LE-NZSP, ME1-NZSP, ME2-NZSP, and HE1-NZSP (Fig. S6). Subsequent bond valence site energy (BVSE) analyses were performed on the DFT-optimized structures to visualize Na^+ diffusion

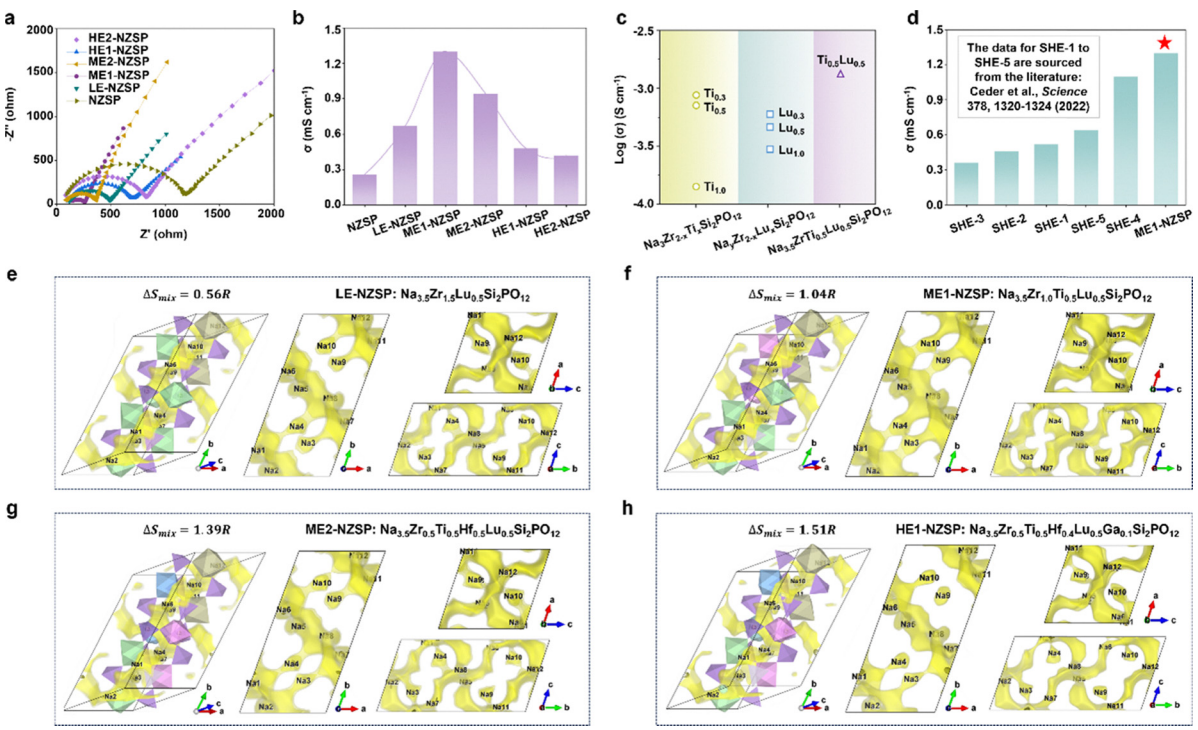

Fig. 5 Ionic conductivity properties of synthesized NASICON oxide SSEs. (a) Room-temperature impedance spectra of the synthesized NASICON oxide SSEs. (b) Comparison of room-temperature ionic conductivity for all synthesized NASICON oxide SSEs. (c) Ionic conductivities of $Na_{3.5}Zr_{1.0}Ti_{0.5}Lu_{0.5}Si_2PO_{12}$ and its single-metal counterparts measured at room temperature. (d) Comparison of ionic conductivity for ME1-NZSP and other medium-to-high entropy NASICON oxide SSEs reported in the literature. (e)–(h) BVSE maps of Na-ion migration pathways in (e) LE-NZSP, (f) ME1-NZSP, (g) ME2-NZSP, and (h) HE1-NZSP: Na^+ probability density isosurfaces of the supercell and different cross-sectional maps.

Open Access Article. Published on 16 janvier 2026. Downloaded on 2026-02-20 16:23:26.
This article is licensed under a Creative Commons Attribution-NonCommercial 3.0 Unported Licence.

pathways. As illustrated in Fig. 5e–h, the resulting energy landscapes demonstrate a strong correlation between the morphology of diffusion channels and the experimentally measured ionic conductivities.

In the low-entropy LE-NZSP (Fig. 5e), the Na^+ diffusion channels are narrow and discontinuous, particularly between Na3 and Na4 sites, resulting in fragmented conduction pathways that hinder long-range ion transport. This structural limitation aligns well with its modest ionic conductivity of 0.67 mS cm^{-1}. In contrast, ME1-NZSP (Fig. 5f) exhibits the most favorable characteristics, including wide and continuous Na^+ diffusion channels that form a well-connected three-dimensional conduction network linking Na3-Na4-Na9-Na10, directly contributing to its superior conductivity of 1.30 mS cm^{-1}. ME2-NZSP (Fig. 5g) displays moderately continuous pathways with minor constrictions near the Na9 site, consistent with its intermediate ionic conductivity of 0.94 mS cm^{-1}. However, when the configurational entropy increases further, the high-entropy composition HE1-NZSP (Fig. 5h) exhibits relatively narrow channels accompanied by irregular discontinuities around several key sites, including Na4, Na9, and Na10. These structural disruptions are likely induced by Ga^{3+}-driven local lattice distortions, which interrupt the continuity of Na^+ migration pathways and limit ionic conductivity despite the high entropy. This phenomenon is consistent with computational insights reported by Ceder's group,[50] where entropy-induced local distortions were shown to modulate the site energy distribution of alkali metal ions. Specifically, moderate local distortions enhance Na^+ transport by increasing overlap among energetically similar sites, thereby forming an efficient percolation network and lowering the activation energy for diffusion. In contrast, excessive distortions disrupt the energy landscape and impair pathway continuity, ultimately reducing ionic mobility.

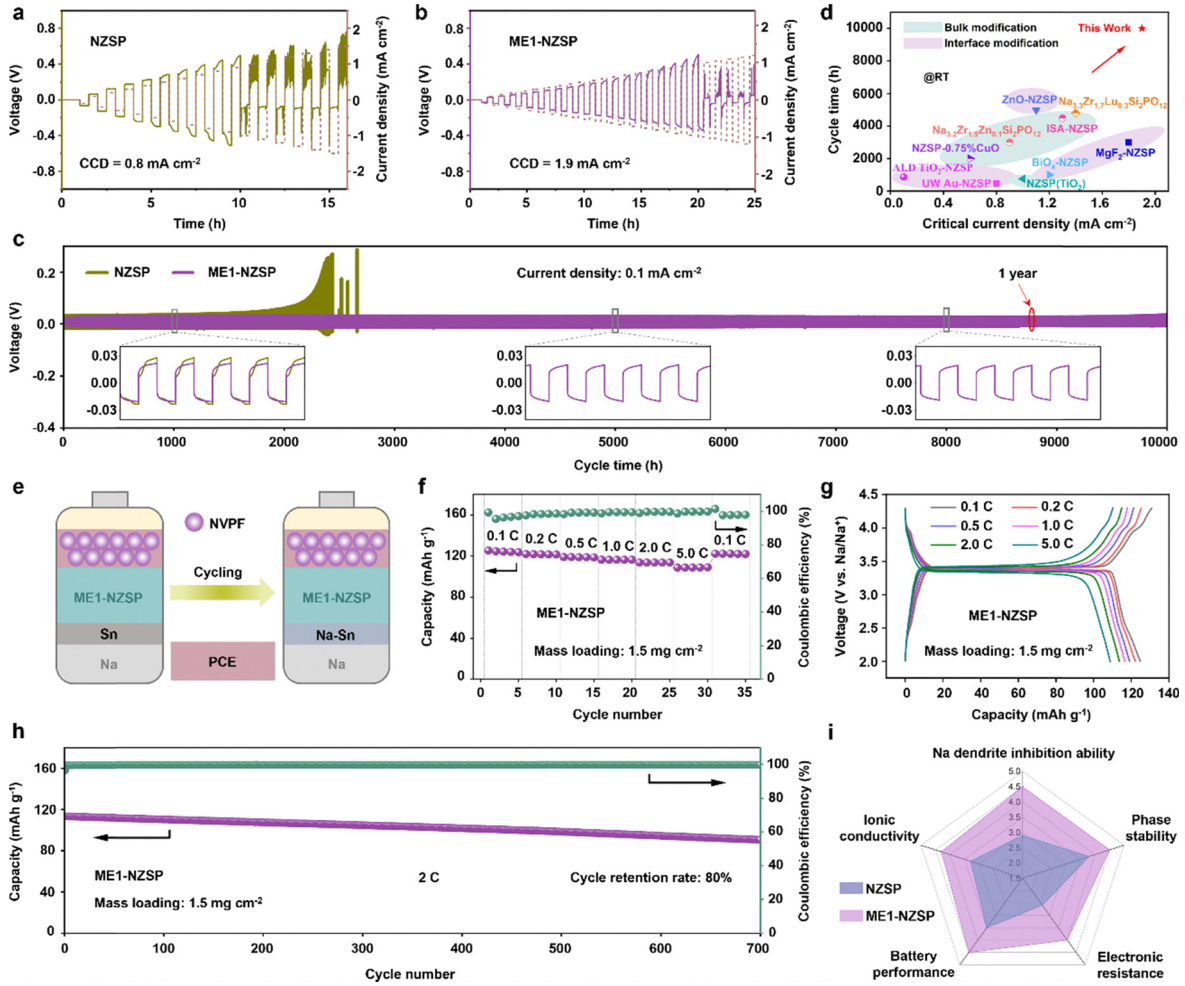

Fig. 6 Electrochemical properties of entropy-stabilized NASICON oxide SSEs. (a) and (b) Galvanostatic cycling of Na symmetric batteries with (a) NZSP and (b) ME1-NZSP SSEs at step-increased current densities. (c) Prolonged galvanostatic cycling of Na symmetric batteries with NZSP and ME1-NZSP SSEs at a current density of 0.1 mA cm^{-2}. (d) Comparison of the critical current density and cycle time of NZSP-based Na symmetrical cells with various modification strategies from recent literature.[13,51–59] (e) Schematic diagram of the ASSSBs assembly. (f) Capacity and Coulombic efficiency at different rates for Na|ME1-NZSP|NVPF ASSSBs at room temperature. (g) Charge and discharge curves of Na|ME1-NZSP|NVPF ASSSBs at different rates at room temperature. (h) Cycling performance of Na|ME1-NZSP|NVPF ASSSBs at 2C and room temperature. (i) Comparison of various properties for NZSP and ME1-NZSP SSEs.

 This journal is © The Royal Society of Chemistry 2026

Open Access Article. Published on 16 janvier 2026. Downloaded on 2026-02-20 16:23:26.
This article is licensed under a Creative Commons Attribution-NonCommercial 3.0 Unported Licence.

Furthermore, the linear shrinkage rates and relative densities of both ME1-NZSP and NZSP pellets were measured subsequent to sintering (Table S9). The pristine NZSP pellet exhibited a low linear shrinkage of 0.9% and a correspondingly low relative density of 85.6%, indicating insufficient densification during sintering. In contrast, the ME1-NZSP pellet showed a significantly higher linear shrinkage of 14.4%, which contributed to its achieving a near-fully dense structure with a relative density of 97.8%. The high relative density and effective densification of ME1-NZSP explain its enhanced ionic conductivity by minimizing grain boundary resistance and ensuring better percolation of ion migration pathways, which aligns with and substantiates the trends observed in our BVSE analysis of the Na-ion migration landscape.

Electrochemical performance of entropy-stabilized NASICON oxide SSE

To demonstrate the practical effectiveness of the synthesized materials, we evaluated the electrochemical performance of ME1-NZSP as a representative entropy-stabilized NASICON oxide SSE. As shown in Fig. S7, DC polarization measurements revealed that ME1-NZSP possesses a significantly lower electronic conductivity (6.45×10^{-9} S cm^{-1}) compared to pristine NZSP (8.49×10^{-8} S cm^{-1}), confirming its excellent insulating nature and suitability for solid-state battery applications. Galvanostatic cycling tests further highlighted the superior interfacial stability and higher critical current density (CCD) of ME1-NZSP. Under stepwise increased current densities ($0.1 \rightarrow 0.8$ mA cm^{-2}), ME1-NZSP maintained stable polarization voltages below 200 mV (Fig. 6b), whereas NZSP exhibited severe voltage fluctuations exceeding 400 mV (Fig. 6a). Long-term cycling at 0.1 mA cm^{-2} demonstrated that ME1-NZSP enabled ultra-stable Na plating/stripping for over 10 000 hours without short-circuiting, while NZSP failed after 2400 hours (Fig. 6c). This remarkable stability is attributed to the entropy-driven homogeneous and dense microstructure (Fig. S8 and Table S9), which effectively suppresses Na dendrite formation by ensuring uniform Na^+ flux and current distribution. Notably, ME1-NZSP achieved a CCD of 1.9 mA cm^{-2}–more than double that of pristine NZSP (0.8 mA cm^{-2}). As summarized in Fig. 6d, ME1-NZSP outperforms most reported NZSP-based SSEs,[13,51–59] including those modified by bulk or interface engineering, demonstrating one of the highest combinations of CCD and cycle life at 0.1 mA cm^{-2} to date.

To further evaluate its practical applicability, we assembled ASSSBs using NVPF as the cathode and Na metal as the anode (Fig. 6e), tested at room temperature. To enhance interfacial contact, a small amount of plastic-crystal electrolyte (PCE) was incorporated into the NVPF cathode composite, while the solid electrolyte surface on the anode side was modified with a Sn coating to form a Na–Sn alloy during cycling, thereby improving Na wettability. As shown in Fig. 6f, the resulting Na|ME1-NZSP|NVPF cells delivered a high discharge specific capacity of 125 mAh g^{-1} at 0.1C with minimal polarization (Fig. 6g). Rate capability measurements further confirmed excellent kinetics, with 88% of the initial capacity retained at 5C. Moreover, as depicted in Fig. 6h, the ASSSBs maintained 80% of their initial capacity after 700 cycles at 2C, significantly outperforming most NZSP-based systems (Table S10). The Coulombic efficiency remained consistently high ($\sim$99.6%) throughout the cycling process, indicating minimal parasitic reactions at the electrode–electrolyte interfaces. A direct comparison between ME1-NZSP and pristine NZSP (Fig. 6i) highlights the multifaceted benefits enabled by entropy engineering, including improved suppression of Na dendrite growth, enhanced phase stability, increased ionic conductivity, reduced electronic conductivity, and overall superior battery performance. These findings collectively emphasize the pivotal role of configurational entropy in optimizing the electrochemical properties of oxide SSEs, positioning ME1-NZSP as a highly promising candidate for next-generation high-energy-density ASSSBs.

Conclusions

In summary, we report a ML-guided strategy for the design of entropy-stabilized NASICON oxide SSEs, overcoming key limitations of phase instability and low ionic conductivity in conventional single-cation systems. By training a GNB model on four descriptors–ionic radius, electronegativity, valence state, and configurational entropy–we efficiently identified four phase-stable multi-cation compositions. Among the synthesized samples, the medium-entropy composition ME1-NZSP demonstrated a high room-temperature Na^+ conductivity of 1.3 mS cm^{-1}, ultra-long-term Na plating/stripping stability (>10 000 h), and a critical current density of 1.9 mA cm^{-2}–outperforming most NASICON-type SSEs. The improved performance is attributed to entropy-induced phase stabilization, which suppresses ZrO_2 impurity formation and enables formation of a pure, conductive NASICON phase. Combined DFT and bond valence analyses reveal that moderate entropy levels create well-connected Na^+ diffusion networks *via* controlled lattice distortions. Practical applicability was validated in Na‖NVPF ASSSBs, which delivered remarkable rate performance (110 mAh g^{-1} at 5C) and impressive cycling stability (80% retention over 700 cycles). This work not only advances NASICON SSE development but also establishes a generalizable ML-entropy co-design framework, paving the way for next-generation SSEs in Na^+, Li^+, K^+, and multivalent-ion batteries.

Author contributions

D. Z., J. T., and Y. S. conceived the idea. D. Z., X. Y., B. P., and T. Y. synthesized the samples, assembled the cells, and performed electrochemical tests. D. Z., J. T., Y. S., and C. X. analyzed all the data involved in the manuscript. X. X., Y. W., and Y. L. examined the XRD, SEM, and TEM information of the samples. T. S., Y. F., J. T., and J. Y. contributed to the ML, BVSE, and DFT data analysis. D. Z, Y. S, H. Z., and S. G. completed the draft manuscript.

Open Access Article. Published on 16 janvier 2026. Downloaded on 2026-02-20 16:23:26.
This article is licensed under a Creative Commons Attribution-NonCommercial 3.0 Unported Licence.

Conflicts of interest

There are no conflicts to declare.

Data availability

The data supporting this article have been included as part of the supplementary information (SI). Supplementary information is available. See DOI: https://doi.org/10.1039/d5ee06594a.

Acknowledgements

This work was financially supported by National Key R&D Program of China (2021YFA1202300), the National Natural Science Foundation of China (52372195, 22503044, 225B2302), the Natural Science Foundation of Jiangsu Province, China (No. BK20240066 and BK20241215), the Guangdong Basic and Applied Basic Research Foundation (2025A1515010043), the Shenzhen Science and Technology Innovation Committee (JCYJ20210324123002008), Shenzhen Science and Technology Program (No.CJGJZD20230724091659001), the Energy Revolution S&T Program of Yulin Innovation Institute of Clean Energy (E411100705), the Jiangsu Funding Program for Excellent Postdoctoral Talent (2024ZB135), and the Jiangsu Province Youth Scientific and Technological Talents Promotion Program (JSTJ-2025-318). We also thank the Nanjing University International Collaboration Initiative.

References

1 X. Zhou, Y. Zhou, L. Yu, L. Qi, K. Oh, P. Hu, S. Lee and C. Chen, *Chem. Soc. Rev.*, 2024, **53**, 5291–5337.
2 W. Zhang, B. Song, M. Wang, T. Miao, X. Huang, E. Zhang, X. Zhan, Y. Yang, H. Zhang and K. Lu, *Energy Environ. Sci.*, 2024, **17**, 5273–5282.
3 D. Wang, B. Gwalani, D. Wierzbicki, V. Singh, L. J. Jhang, T. Rojas, R. Kou, M. Liao, L. Ye, H. Jiang, S. Shan, A. Silver, A. T. Ngo, Y. Du, X. Li and D. Wang, *Nat. Mater.*, 2025, **24**, 243–251.
4 J. Cui, R. Zou, W. Zhang, H. Wen, J. Liu, S. Wang, S. Liu, H. Chen, W. Liu, X. Ju, W. Wang, T. Gan, J. Li, J. Guo, T. He, H. Cao and P. Chen, *Nature*, 2025, **646**, 338–342.
5 R. Sun, R. Zhu, J. Li, Z. Wang, Y. Zhu, L. Yin, C. Wang, R. Wang and Z. Zhang, *Carbon Neutralization*, 2024, **3**, 597–605.
6 Y. Yang, S. Yang, X. Xue, X. Zhang, Q. Li, Y. Yao, X. Rui, H. Pan and Y. Yu, *Adv. Mater.*, 2024, **36**, 2308332.
7 S. Lou, F. Zhang, C. Fu, M. Chen, Y. Ma, G. Yin and J. Wang, *Adv. Mater.*, 2021, **33**, 2000721.
8 G. Liu, J. Yang, J. Wu, Z. Peng and X. Yao, *Adv. Mater.*, 2024, **36**, 2311475.
9 X. Wang, C. Zhang, M. Sawczyk, J. Sun, Q. Yuan, F. Chen, T. C. Mendes, P. C. Howlett, C. Fu, Y. Wang, X. Tan, D. J. Searles, P. Král, C. J. Hawker, A. K. Whittaker and M. Forsyth, *Nat. Mater.*, 2022, **21**, 1057–1065.
10 X. Lin, S. Zhang, M. Yang, B. Xiao, Y. Zhao, J. Luo, J. Fu, C. Wang, X. Li, W. Li, F. Yang, H. Duan, J. Liang, B. Fu, H. Abdolvand, J. Guo, G. King and X. Sun, *Nat. Mater.*, 2025, **24**, 83–91.
11 M. Wu, X. Liu, H. Liu, D. Li, X. Qi, J. Zeng, L. Gao, C.-W. Nan and L.-Z. Fan, *Nat. Commun.*, 2025, **16**, 2808.
12 Y. Li, Z. Wang, C. Sun, S. Liu, Y. Dou, X. Yuan, H. Jin and Y. Zhao, *Adv. Funct. Mater.*, 2025, **35**, 2425995.
13 D. Zuo, L. Yang, Z. Zou, S. Li, Y. Feng, S. J. Harris, S. Shi and J. Wan, *Adv. Energy Mater.*, 2023, **13**, 2301540.
14 H. An, M. Li, Q. Liu, Y. Song, B. Deng, X. Liu and J. Wang, *Nat. Sustainable*, 2025, **8**, 661–671.
15 X. Wang, Y. Fan, J. Li, X. Li, W. Li, J. Wang and W. K. Pang, *Energy Environ. Sci.*, 2025, **18**, 1096–1129.
16 X. Feng, H. Fang, N. Wu, P. Liu, P. Jena, J. Nanda and D. Mitlin, *Joule*, 2022, **6**, 543–587.
17 D. N. Karmalkar, D. Dutta, A. K. Bera, S. M. Yusuf and B. Pahari, *J. Phys. Chem. C*, 2024, **128**, 768–777.
18 Y. B. Rao and L. N. Patro, *Mater. Lett.*, 2021, **301**, 130267.
19 P. Jiang, G. Du, Y. Shi, F. She, P. Guo, G. Qian, X. Lu, F. Xie and X. Lu, *Chem. Eng. J.*, 2023, **451**, 138771.
20 X. Wang, Z. Liu, Y. Tang, J. Chen, D. Wang and Z. Mao, *J. Power Sources*, 2021, **481**, 228924.
21 S. Rizvi, I. Aladhyani, Y. Ding and Q. Zhang, *Nano Energy*, 2024, **129**, 110009.
22 J. Luo, G. Zhao, W. Qiang and B. Huang, *J. Am. Ceram. Soc.*, 2022, **105**, 3428–3437.
23 J. Yang, G. Liu, M. Avdeev, H. Wan, F. Han, L. Shen, Z. Zou, S. Shi, Y.-S. Hu, C. Wang and X. Yao, *ACS Energy Lett.*, 2020, **5**, 2835–2841.
24 X. Wang, J. Chen, Z. Mao and D. Wang, *Chem. Eng. J.*, 2022, **427**, 130899.
25 F. Ding, Y. Lu, L. Chen and Y.-S. Hu, *Electrochem. Energy Rev.*, 2024, **7**, 16.
26 M. Ali, M. Saleem, T. Sattar, M. Z. Khan, J. H. Koh, O. Gohar, I. Hussain, Y. Zhang, M. B. Hanif, G. Ali and M. F. Khan, *Mater. Sci. Eng., R*, 2025, **163**, 100921.
27 Y. Liu, P. Tuo, F. Z. Dai, Z. Yu, W. Lai, Q. Ding, P. Yan, J. Gao, Y. Hu, Y. Hu, Y. Fan and W. Jiang, *Adv. Mater.*, 2024, **36**, 2400059.
28 R. Zhang, S. Zhao, J. Ding, Y. Chong, T. Jia, C. Ophus, M. Asta, R. O. Ritchie and A. M. Minor, *Nature*, 2020, **581**, 283–287.
29 W.-L. Hsu, C.-W. Tsai, A.-C. Yeh and J.-W. Yeh, *Nat. Rev. Chem.*, 2024, **8**, 471–485.
30 Y. Mu, R. Ma, S. Xue, H. Shang, W. Lu and L. Jiao, *Carbon Neutralization*, 2024, **3**, 4–31.
31 C. Oses, C. Toher and S. Curtarolo, *Nat. Rev. Mater.*, 2020, **5**, 295–309.
32 S. Divilov, H. Eckert, D. Hicks, C. Oses, C. Toher, R. Friedrich, M. Esters, M. J. Mehl, A. C. Zettel, Y. Lederer, E. Zurek, J.-P. Maria, D. W. Brenner, X. Campilongo, S. Filipović, W. G. Fahrenholtz, C. J. Ryan, C. M. DeSalle, R. J. Crealese, D. E. Wolfe, A. Calzolari and S. Curtarolo, *Nature*, 2024, **625**, 66–73.
33 H. Li, X. Sun and H. Huang, *Prog. Mater. Sci.*, 2025, **148**, 101382.

 This journal is © The Royal Society of Chemistry 2026

Open Access Article. Published on 16 janvier 2026. Downloaded on 2026-02-20 16:23:26.
This article is licensed under a Creative Commons Attribution-NonCommercial 3.0 Unported Licence.

34 Z. Zhou, Y. Ma, T. Brezesinski, B. Breitung, Y. Wu and Y. Ma, *Energy Environ. Sci.*, 2025, **18**, 19–52.
35 M. Sun, Y. Sun, H. Ma, S. Wang, Q. Liu, G. Zhao, L. Duan, Q. Hu, Q. An, K. Zeng, W. Huang, X. Zou, Y. Yang and H. Guo, *ACS Nano*, 2025, **19**, 18386–18396.
36 Z. Hao, X. Shi, W. Zhu, Z. Yang, X. Zhou, C. Wang, L. Li, W. Hua, C.-Q. Ma and S. Chou, *ACS Nano*, 2024, **18**, 9354–9364.
37 X. H. Wu, W. J. Jiang, C. Dai, L. Z. Liu, Y. Chai, M. J. Zhao, L. B. Yang, Y. Lin, Y. Zhao and W. Huang, *Adv. Mater.*, 2025, **37**, 2414358.
38 A. C. C. Dutra, B. A. Goldmann, M. S. Islam and J. A. Dawson, *Nat. Rev. Mater.*, 2025, **10**, 566–583.
39 B. Wang, H. A. Doan, S.-B. Son, D. P. Abraham, S. E. Trask, A. Jansen, K. Xu and C. Liao, *Nat. Commun.*, 2025, **16**, 3413.
40 H. Xin, *Nat. Energy*, 2022, **7**, 790–791.
41 P. Yin, X. Niu, S.-B. Li, K. Chen, X. Zhang, M. Zuo, L. Zhang and H.-W. Liang, *Nat. Commun.*, 2024, **15**, 415.
42 H. Liu, J. Li, J. Arbiol, B. Yang and P. Tang, *EcoEnergy*, 2023, **1**, 154–185.
43 J. Xu and E. H. Sargent, *Nat. Mater.*, 2023, **22**, 1449–1450.
44 S. Lu, Q. Zhou, Y. Ouyang, Y. Guo, Q. Li and J. Wang, *Nat. Commun.*, 2018, **9**, 3405.
45 P. Hudon and D. R. Baker, *J. Non-Cryst. Solids*, 2002, **303**, 299–345.
46 S. F. Matar and G. Campet, *J. Phys. Chem. Solids*, 2007, **68**, 331–336.
47 A. W. Sleight, *Prog. Solid State Chem.*, 2009, **37**, 251–261.
48 L. K. Bhaskar, V. Nallathambi and R. Kumar, *J. Am. Ceram. Soc.*, 2020, **103**, 3416–3424.
49 A. Sarkar, Q. Wang, A. Schiele, M. R. Chellali, S. S. Bhattacharya, D. Wang, T. Brezesinski, H. Hahn, L. Velasco and B. Breitung, *Adv. Mater.*, 2019, **31**, 1806236.
50 Y. Zeng, B. Ouyang, J. Liu, Y.-W. Byeon, Z. Cai, L. J. Miara, Y. Wang and G. Ceder, *Science*, 2022, **378**, 1320–1324.
51 J. Yang, Z. Gao, T. Ferber, H. Zhang, C. Guhl, L. Yang, Y. Li, Z. Deng, P. Liu, C. Cheng, R. Che, W. Jaegermann, R. Hausbrand and Y. Huang, *J. Mater. Chem. A*, 2020, **8**, 7828–7835.
52 H. Liu, Y. Xing, N. Chen, J. Wu, Y. Li and C. Zhang, *Chem. Mater.*, 2023, **35**, 8686–8694.
53 B. Wei, S. Huang, X. Wang, M. Liu, C. Huang, R. Liu and H. Jin, *Energy Environ. Sci.*, 2025, **18**, 831–840.
54 R. Wang, W. Feng, X. Yu, Q. Shi, P. Wang, Y. Liu, J. Zhang and Y. Zhao, *eScience*, 2024, **4**, 100274.
55 D. Fang, Y. Li, C. Wang, R. Miao, S. Yang, Y. Zhao, Y. Ding, J. He, L. Chen, N. Li, J. Li, Y. Su and H. Jin, *Energy Storage Mater.*, 2025, **42**, 103973.
56 Z. Gao, J. Yang, G. Li, T. Ferber, J. Feng, Y. Li, H. Fu, W. Jaegermann, C. W. Monroe and Y. Huang, *Adv. Energy Mater.*, 2022, **12**, 2103607.
57 Z. Sun, L. Li, C. Sun, Q. Ni, Y. Zhao, H. Wu and H. Jin, *Nano Lett.*, 2022, **22**, 7187–7194.
58 D. Li, X. Wang, Q. Guo, X. Yu, S. Cen, H. Ma, J. Chen, D. Wang, Z. Mao and C. Dong, *Carbon Energy*, 2023, **5**, e299.
59 Q. Ni, Y. Ding, C. Wang, S. Bai, K. Zhu, Y. Zhao, L. Chen, N. Li, J. Li, Y. Su and H. Jin, *Adv. Mater.*, 2024, **36**, 2309298.